Kinetic and mechanistic aspects of hydroxyl radical–mediated degradation of naproxen and reaction intermediates

Shuang Luo [a, b], Lingwei Gao [a, b], Zongsu Wei [c], Richard Spinney [d], Dionysios D. Dionysiou [e], Wei-Ping Hu [f], Liyuan Chai [a, b], Ruiyang Xiao [a, b, *]

[a] Institute of Environmental Engineering, School of Metallurgy and Environment, Central South University, Changsha, 410083, China
[b] Chinese National Engineering Research Center for Control & Treatment of Heavy Metal Pollution, Changsha, 410083, China
[c] Laboratory for the Chemistry of Construction Materials (LC²), Department of Civil and Environmental Engineering, University of California, Los Angeles, CA, 90095, USA
[d] Department of Chemistry and Biochemistry, The Ohio State University, Columbus, OH, 43210, USA
[e] Environmental Engineering and Science Program, Department of Chemical and Environmental Engineering (ChEE), University of Cincinnati, Cincinnati, OH, 45221, USA
[f] Department of Chemistry and Biochemistry, National Chung Cheng University, Chia–Yi, 62102, Taiwan

ARTICLE INFO

ABSTRACT

Hydroxyl radical ($^{\bullet}$OH) based advanced oxidation technologies (AOTs) are effective for removing non–steroidal anti–inflammatory drugs (NSAIDs) during water treatment. In this study, we systematically investigated the degradation kinetics of naproxen (NAP), a representative NSAID, with a combination of experimental and theoretical approaches. The second–order rate constant (k) of $^{\bullet}$OH oxidation of NAP was measured to be $(4.32 \pm 0.04) \times 10^9 \, M^{-1} \, s^{-1}$, which was in a reasonable agreement with transition state theory calculated k value ($1.08 \times 10^9 \, M^{-1} \, s^{-1}$) at SMD/M05−2X/6−311++G**//M05−2X/6−31+G** level of theory. The calculated result revealed that the dominant reaction intermediate is 2–(5–hydroxy–6–methoxynaphthalen–2–yl)propanoic acid (HMNPA) formed via radical adduct formation pathway, in which $^{\bullet}$OH addition onto the ortho site of the methoxy–substituted benzene ring is the most favorable pathway for the NAP oxidation. We further investigated the subsequent $^{\bullet}$OH oxidation of HMNPA via a kinetic modelling technique. The k value of the reaction of HMNPA and $^{\bullet}$OH was determined to be $2.22 \times 10^9 \, M^{-1} \, s^{-1}$, exhibiting a similar reactivity to the parent NAP. This is the first study on the kinetic and mechanistic aspects of NAP and its reaction intermediates. The current results are valuable in future study evaluating and extending the application of $^{\bullet}$OH based AOTs to degrade NAP and other NSAIDs of concern in water treatment plants.

1. Introduction

Non–steroidal anti–inflammatory drugs (NSAIDs) are widely used in relieving pain, reducing fever and inhibiting inflammation (Kosjek et al., 2005; Zhang et al., 2017). They have been frequently detected in influent of municipal wastewater treatment plant (WWTP) (Benitez et al., 2011). Naproxen (NAP), one of the best–selling NSAIDs, is a propionic acid derivative with a naphthalene ring and methoxy group. It was found with concentrations ranging from 0.1 ng L^{-1} to 7.69 μg L^{-1} in the WWTP effluents and 0.1–0.25 μg L^{-1} in surface water (Benotti et al., 2008; Boyd et al., 2005). Despite such low measured concentrations (from ng L^{-1} to μg L^{-1}) in water environment, their potential threat to aquatic organisms cannot be ignored (Luo et al., 2017a; Zhou et al., 2017). The toxicological studies demonstrate that NAP exhibits adverse effects on aquatic organisms with an EC$_{50}$ of 21.2 μg L^{-1} on *Vibrio fischeri* (Balakrishna et al., 2017). In addition, ingestion of trace amounts of NAP for long periods of time can cause humans to suffer a higher risk of heart attack (Manrique-Moreno et al., 2010). However, these compounds cannot be completely removed by activated sludge–based wastewater treatment technology due to their low bioavailability and biodegradability. They reach surface and ground waters though wastewater effluent discharge (Lapworth et al., 2012). Therefore, it is urgent to develop an effective removal

technology for these contaminants in wastewater treatment processes.

The removal of NAP ranging from 1.4 to 4.8 μg L^{-1} was not effective by the means of traditional sedimentation and adsorption as it was shown no significant reduction in NAP concentrations in a municipal wastewater treatment plant (Carballa et al., 2004). Tang et al. (2014) investigated the removal efficiency of NAP in the presence of activated sludge under aerobic conditions. The removal efficiency was only 14.8−26.0% for the initial concentrations of 10−200 μg L^{-1} with 1 h of contact time. By comparison, advanced oxidation technologies (AOTs) that form free radicals (e.g. hydroxyl radical, $^{\bullet}$OH, or sulfate radical, SO$_4^{\bullet-}$) at ambient temperature and atmospheric pressure were demonstrated to be effective for removal of those organic contaminants in waters (Ghernaout, 2013; Xiao et al., 2017). Hydroxyl radical attacks most of the organic compounds with high second−order rate constants (k), a key factor to estimate degradation kinetics and removal efficiency (Buxton et al., 1988). Although AOTs for removal of NAP have been reported (Feng et al., 2013; Huber et al., 2005), little is known about mechanistic aspects of NAP degradation, particularly the contribution of each reaction pathway (i.e., radical adduct formation (RAF), hydrogen atom transfer (HAT), and single electron transfer (SET)) to the overall degradation. Further, it remains challenging to obtain this kind of mechanistic evidence from experiments due to the lack of analytical methods that enable comprehensive characterization of the reaction intermediates.

The density functional theory (DFT) approach features many advantages in calculating thermodynamic and kinetic behaviors in biomolecular reactions between radical and non−radical species (Luo et al., 2017b; Yang et al., 2016; Ye et al., 2017). Mounting evidences show that DFT designed for thermochemical kinetics represents a good balance between computational cost and performance (Galano and Alvarez-Idaboy, 2013; Xiao et al., 2014, 2015a). For example, Xiao et al. (2017) investigated the k value between $^{\bullet}$OH and bisphenol A (BPA) based on a combination of experimental and computational methods at M05–2X level of theory. The HAT pathway accounted for 85.7% of the overall k value in $^{\bullet}$OH oxidation reaction of BPA. They concluded that the quinone of monohydroxylated BPA was the dominant reaction intermediate, which has been verified by many studies (Dai et al., 2016; Sharma et al., 2016).

It should be noted that more and more studies indicate that reaction intermediates play an important role during the AOT process (An et al., 2013; Du et al., 2006). For example, Du et al. (2006) investigated the reaction intermediates in the degradation of 4−chlorophenol, 4−nitrophenol and phenol by Fenton reaction. The hydroquinone–like reaction intermediates quenched/ competed for $^{\bullet}$OH, and thus were considered to be an important process in controlling the overall removal rate of target contaminants. Therefore, understanding formation kinetics of reaction intermediates will enhance our knowledge of mechanisms on $^{\bullet}$OH oxidation of organic contaminants and practically guide the application of AOTs.

In this study, experimental, theoretical, and kinetic modelling approaches were combined to investigate the thermodynamics and kinetics of $^{\bullet}$OH oxidation of NAP and its dominant intermediate. First, the relative rate method was used to experimentally determine the k value for the reaction of $^{\bullet}$OH and NAP. In the following theoretical calculation, the energy profiles of RAF, HAT and SET reaction pathways between NAP and $^{\bullet}$OH were investigated by the DFT approach. Further, a kinetic modelling technique was used to simulate concentration evolution of NAP and its dominant intermediate through the course of reaction. The k value between the reaction intermediate and $^{\bullet}$OH was reported and compared with the experimental measurement. This study shed light on the

mechanisms of $^{\bullet}$OH oxidation of NAP and the role of degradation intermediates in the $^{\bullet}$OH based AOTs in advanced water treatment.

2. Materials and methods

2.1. Materials

Naproxen (NAP, >99%), H$_3$PO$_4$ (85−90%), Na$_2$HPO$_4$ (99%), NaH$_2$PO$_4$ (99%), and acetophenone (ACP, >99%) were purchased from Sigma–Aldrich and used without further purification. H$_2$O$_2$ (30% by weight), H$_2$SO$_4$ (guaranteed reagent), KMnO$_4$ (analytical grade), and Na$_2$C$_2$O$_4$ (analytical grade) were purchased from Sinopharm Chemical Reagent, China. H$_3$PO$_4$, Na$_2$HPO$_4$ and NaH$_2$PO$_4$ were used as buffer system. H$_2$O$_2$ was used as precursor to generate $^{\bullet}$OH under UV irradiation. H$_2$SO$_4$, KMnO$_4$ and Na$_2$C$_2$O$_4$ were used for average light intensity per volume (I_0) and optical path (l) measurements. ACP was chosen as a reference compound to determine the k value of $^{\bullet}$OH oxidation of NAP based on our previous studies (Xiao et al., 2017; Yang et al., 2017). The physicochemical properties of NAP are listed in Table A1 (see supplemental information). All solutions were prepared using deionized (DI) water from a Molecular water system (Molresearc 1010A). The S220 pH meter (Mettler Toledo) was used to measure solution pH.

2.2. Photochemical experiments

The degradation kinetic experiments were performed in a merry−go−round photochemical reactor, which was greatly modified from a commercial reactor (XPA−7, Xujiang Technology Co., Ltd. Nanjing, China) (Fig. A1). A 10 W low pressure UV lamp (GPH212T5L/4, Heraeus) in a quartz trap was centered in 50 mL quartz reaction tubes. These reaction tubes were immersed in constant temperature tank at 20 ± 1 °C maintained by a water cooling system (SC150−A25B, Thermo Fisher Scientific). The solutions in reaction tubes were continuously stirred by a Teflon magnetic bar. The initial concentrations of NAP, ACP and H$_2$O$_2$ in the UV/ H$_2$O$_2$ system were prepared at 10 μM, 10 μM, and 100 μM, respectively. Solution pH was buffered at pH = 3.0 in a 10 mM phosphate buffer system. The majority (i.e., 93.5%) of NAP species is in its neutral form at pH 3 based on its acid dissociation constant (pK_a = 4.15) (Broséus et al., 2009). The sample of 0.6 mL was taken from the reactors using a 2.5 mL glass syringe (Gastight 1001, Hamilton). The I_0 and l were determined using potassium permanganate titration and UV spectrophotometry, respectively (Xiao et al., 2017).

The molar absorption coefficients (ε, M^{-1} cm^{-1}) and quantum yield (φ, mol Einstein^{-1}) are the key factors to determine direct photolysis at a given wavelength (Chuang et al., 2016; Zepp, 1978). The ε and φ values reflect the capability of a compound to utilize photon. Based on the Beer−Lambert law, the initial rate of direct photolysis of NAP (r_{UV}, M min^{-1}) can be determined as:

$$r_{UV} = -\frac{dC}{dt} = \varphi I_0 \left(1 - 10^{-\varepsilon l C} \right) \tag{1}$$

where I_0 is the lamp irradiance, which was measured to be 1.89 × 10^{-6} Einstein L^{-1} s^{-1} in this study; l is the effective optical path length (1.04 cm); C is concentration of NAP (M); and ε is the molar absorption coefficient (M^{-1} cm^{-1}) which can be calculated from the total absorbance (A, cm^{-1}) measured by spectrophotometer at 254 nm.

$$\varepsilon = \frac{A}{b\,C} \tag{2}$$

where b is the path length of quartz cuvette (1 cm). The ε value in our system was determined to be $4500\,M^{-1}\,cm^{-1}$ at 254 nm (Fig. A2). The value was similar to the reported values by Pereira et al. (2007) ($4900\,M^{-1}\,cm^{-1}$) and Marotta et al. (2013) ($4180\,M^{-1}\,cm^{-1}$).

The φ value of NAP was calculated according to eqn. (3):

$$\varphi = \frac{r_{UV}}{I_0 \times (1 - 10^{-\varepsilon \times l \times C})} \quad (3)$$

The relative rate technique was used to determine the second−order rate constant (k) value of the reaction between NAP and $^{\bullet}OH$. The ACP has been successfully used as a reference compound in a UV/H_2O_2 system to determine the k values for various organic pollutants (Packer et al., 2003). The k_{ACP} value of NAP reacting with $^{\bullet}OH$ was reported to be $5.9 \times 10^9\,M^{-1}\,s^{-1}$ at pH 3 (Buxton et al., 1988), but its degradation kinetics of UV direct photolysis was slow. The ACP is neither acidic nor basic and does not protonate/deprotonate with pH, thus it is applicable in a wide pH range; further, the k value ($5.9 \times 10^9\,M^{-1}\,s^{-1}$) is at the level of the same order of magnitude with the k values of some drugs reacting with $^{\bullet}OH$ (Yang et al., 2017). k_{NAP} value was calculated according to eqn. (4).

$$\frac{k_{NAP}}{k_{ACP}} = \frac{\ln\frac{[NAP]_t}{[NAP]_0} - \left(\ln\frac{[NAP]_t}{[NAP]_0}\right)_{UV}}{\ln\frac{[ACP]_t}{[ACP]_0} - \left(\ln\frac{[ACP]_t}{[ACP]_0}\right)_{UV}} = \frac{\ln\frac{[NAP]_t}{[NAP]_0} - k'_{NAP,\,UV}}{\ln\frac{[ACP]_t}{[ACP]_0} - k'_{ACP,\,UV}} \quad (4)$$

where $k'_{NAP,\,UV}$ and $k'_{ACP,\,UV}$ are the first–order rate constants (min^{-1}) of UV direct photolysis of NAP and ACP, respectively. All photolysis experiments were carried out in duplicate.

2.3. Analytical methods

Quantitative analysis of NAP and ACP was performed using an ultra–performance liquid chromatography (Waters ACQUITY H–Class) with BEH C18 column (1.7 μm, 50 × 2.1 mm, Waters). The column temperature was set at 35 °C, and sample injection volume was 5 μL. The mobile phase with a flow rate of 0.3 mL min^{-1} consisted of 35% acetonitrile and 65% phosphoric buffer (20 mM at pH 3). The absorption wavelengths of NAP and ACP were set at 229 nm and 255 nm, respectively. The absorption spectrum of NAP was measured by a UV–1800 spectrometer (Shimadzu, Japan) from 200 to 400 nm to determine the maximum absorption.

2.4. Theoretical computational methods

The DFT approach was used to calculate the energetics of different reaction pathways between $^{\bullet}OH$ and NAP. First, the global minimum energy geometry of NAP was located by a conformation search with MMFF force field using the Spartan' 10 program (Tonelli, 2014). The geometries of the reactants, products and transition state (TS) were then optimized using Gaussian 09 (Revision A.01) (Frisch et al., 2009) at M05–2X/6–31 + G** level of theory (Zhao and Truhlar, 2008). All the local minima of reactants and products have positive vibration frequencies, and TS species have only one imaginary frequency (see Table A2–A15 for co-ordinates) (Dreuw, 2005). The energies of all the species were calculated at the M05–2X/6–311++ G** level of theory with the solvation model of density (SMD) continuum solvation model (Zhao et al., 2006). The SMD model is considered to be a reliable solvation model due to its applicability to both charged and un-charged solutes in water (Marenich et al., 2009). The distribution of highest occupied molecular orbital (HOMO) and lowest unoc-cupied molecular orbital (LUMO) characterizes the chemical reactivity and charge transfer interaction in the molecule (Sethi et al., 2017).

The conventional transition state theory (TST) was also used to calculate the k value at the molecular level (Truhlar et al., 1996):

$$k = \sigma \Gamma \frac{k_B T}{h} e^{-(\Delta^{\ddagger}G^{\circ})/RT} \quad (5)$$

where k_B and h are the Boltzmann and Planck constants, respectively, R is the ideal gas constant ($8.314\,J\,mol^{-1}\,K^{-1}$), $\Delta^{\ddagger}G^{\circ}$ is the Gibbs free energy of activation, σ represents the reaction path de-generacy, Γ is the tunneling correction factor by Eckart's approach (Brown, 1981; Xiao et al., 2014). The diffusion–limited rate con-stants (k_D) was used to correct the TST calculated k values (k_{TST}) based on the Collins−Kimball diffusion limit theory (Collins and Kimball, 1949):

$$k_{correction} = \frac{k_{TST} k_D}{k_{TST} + k_D} \quad (6)$$

k_D can be calculated by the Smoluchowski equation for an irre-versible bimolecular diffusion–controlled reaction in aqueous so-lution. The k_D calculation is detailed elsewhere (An et al., 2013; Xiao et al., 2017). The branching ratio (θ_i, %) represents the percent of the contribution of each reaction pathway (i) to the overall k value:

$$\theta = \frac{k_i}{k_{overall}} \quad (7)$$

2.5. Kinetic modelling

Kinetic modelling has been successfully used to model kinetics of $^{\bullet}OH$ oxidation of organic contaminants, and were elaborated in previous studies in detail (Chuang et al., 2016; Lian et al., 2017). The relevant reactions occurred in the UV/H_2O_2 system are listed in Table 1. Among the 26 reactions, 23 k values were obtained from literature. The formation rate (s^{-1}) of $^{\bullet}OH$ in our system was measured. The k values for rxn (abbreviation for reaction) #25 (i.e., $^{\bullet}OH$ oxidation of NAP) and #26 (i.e., $^{\bullet}OH$ oxidation of the dominant intermediate), and their concentration evolution were fit by the kinetic model. The k value fitting was derived from the mass balance of the target species (Chuang et al., 2016; Tonelli, 2014). The kinetic model was built with MATLAB (Version 8.0) and Kintecus (Version 6.0) (Ianni, 2017). Briefly, in order to roughly estimate the range of k values of rxn #25 and #26, the MATLAB program was first used to solve the system of differential equations to simulate NAP concentration evolution based on the experimental observation. The range of k values of rxn #25 and #26 were determined to be approximately $5 \times 10^9 \sim 10^{10}\,M^{-1}\,s^{-1}$. In addition to the input information of reactions such as interval time, H_2O_2 concentration, etc., the estimated k values were fed to Kintecus to simultaneously optimize k values and NAP concen-tration evolution. The Kintecus program offers a combination of five types of optimization algorithms (Mead & Nelder, Powerll, Levenberg−Marquardt, simulated annealing, and complex method) and three comparison operators (relative least squares, standard least squares, and Ianni function) to fit the kinetic data (Ianni, 2017).

3. Results and discussion

3.1. UV direct photolysis of NAP

UV direct photolysis was first monitored to evaluate its

Table 1
Reactions and their k values for the $^\bullet$OH oxidation of NAP in this study.

#	Reaction	k	Reference
1	$H_2O_2 + h\nu \rightarrow 2\ ^\bullet OH$	$8.39 \times 10^{-5}\,s^{-1}$	determined in study
2	$H_2O \rightarrow H^+ + OH^-$	$1.0 \times 10^{-3}\,s^{-1}$	(Grebel et al., 2010)
3	$H^+ + OH^- \rightarrow H_2O$	$1.0 \times 10^{11}\,M^{-1}\,s^{-1}$	(Grebel et al., 2010)
4	$H_2O_2 \rightarrow HO_2^- + H^+$	$1.3 \times 10^{-1}\,s^{-1}$	(Grebel et al., 2010)
5	$HO_2^- + H^+ \rightarrow H_2O_2$	$5.0 \times 10^{10}\,M^{-1}\,s^{-1}$	(Grebel et al., 2010)
6	$^\bullet OH + H_2O_2 \rightarrow HO_2^\bullet + H_2O$	$2.7 \times 10^{7}\,M^{-1}\,s^{-1}$	(Buxton et al., 1988)
7	$H_2O_2 + HO_2^\bullet \rightarrow\ ^\bullet OH + H_2O + O_2$	$3.0\,M^{-1}\,s^{-1}$	(Koppenol et al., 1978)
8	$HO_2^\bullet \rightarrow O_2^{\bullet -} + H^+$	$7.0 \times 10^{5}\,s^{-1}$	(Liang et al., 2006)
9	$O_2^{\bullet -} + H^+ \rightarrow HO_2^\bullet$	$5.0 \times 10^{10}\,M^{-1}\,s^{-1}$	(Liang et al., 2006)
10	$H_2O_2 + O_2^{\bullet -} \rightarrow\ ^\bullet OH + OH^- + O_2$	$0.13\,M^{-1}\,s^{-1}$	(Crittenden et al., 1999)
11	$HO_2^\bullet + O_2^{\bullet -} \rightarrow HO_2^- + O_2$	$9.7 \times 10^{7}\,M^{-1}\,s^{-1}$	(Bielski et al., 1985)
12	$HO_2^\bullet + HO_2^\bullet \rightarrow H_2O_2 + O_2$	$8.3 \times 10^{5}\,M^{-1}\,s^{-1}$	(Bielski et al., 1985)
13	$^\bullet OH +\ ^\bullet OH \rightarrow H_2O_2$	$5.5 \times 10^{9}\,M^{-1}\,s^{-1}$	(Buxton et al., 1988)
15	$^\bullet OH + OH^- \rightarrow H_2O + O_2^{\bullet -}$	$1.2 \times 10^{10}\,M^{-1}\,s^{-1}$	(Buxton et al., 1988)
15	$^\bullet OH + HO_2^\bullet \rightarrow H_2O + O_2$	$7.1 \times 10^{9}\,M^{-1}\,s^{-1}$	(Buxton et al., 1988)
16	$^\bullet OH + O_2^{\bullet -} \rightarrow OH^- + O_2$	$1.0 \times 10^{10}\,M^{-1}\,s^{-1}$	(Liang et al., 2006)
17	$^\bullet OH + HO_2^- \rightarrow H_2O + O_2^{\bullet -}$	$7.5 \times 10^{9}\,M^{-1}\,s^{-1}$	(Christensen et al., 1982)
18	$^\bullet OH + HO_2^- \rightarrow HO_2^\bullet + OH^-$	$7.5 \times 10^{9}\,M^{-1}\,s^{-1}$	(Christensen et al., 1982)
19	$2H_2O_2 \rightarrow 2H_2O + O_2$	$2.3 \times 10^{-2}\,s^{-1}$	(Grebel et al., 2010)
20	$^\bullet OH + H_3PO_4 \rightarrow H_2PO_4^\bullet + H_2O$	$2.7 \times 10^{6}\,M^{-1}\,s^{-1}$	(Buxton et al., 1988)
21	$^\bullet OH + H_2PO_4^- \rightarrow H_2PO_4^\bullet + OH^-$	$2.0 \times 10^{4}\,M^{-1}\,s^{-1}$	(Buxton et al., 1988)
22	$^\bullet OH + HPO_4^{2-} \rightarrow HPO_4^{\bullet -} + OH^-$	$1.5 \times 10^{5}\,M^{-1}\,s^{-1}$	(Buxton et al., 1988)
23	$^\bullet OH + PO_4^{3-} \rightarrow PO_4^{\bullet 2-} + OH^-$	$<1.0 \times 10^{7}\,M^{-1}\,s^{-1}$	(Buxton et al., 1988)
24	$H_2O_2 + HPO_4^{\bullet -} \rightarrow H_2PO_4^- + HO_2^\bullet$	$2.7 \times 10^{7}\,M^{-1}\,s^{-1}$	(Crittenden et al., 1999)
25	$^\bullet OH + NAP \rightarrow$ products	$2.5 \times 10^{9}\,M^{-1}\,s^{-1}$	fitted
26	$^\bullet OH + HMNPA \rightarrow$ product	$2.2 \times 10^{9}\,M^{-1}\,s^{-1}$	fitted

Note: $[H_3PO_4]$, $[H_2PO_4^-]$, $[H_2PO_4^{2-}]$ and $[PO_4^{3-}]$ were detemined to be 1.29×10^{-3}, 8.66×10^{-3}, 5.34×10^{-7}, $2.38 \times 10^{-16}\,M$, respectively at pH = 3 in our system.

influence on total degradation of NAP. The r_{UV} of NAP was measured to be $(2.32 \pm 0.12) \times 10^{-7}\,M\,min^{-1}$ at the initial concentration of $10\,\mu M$. The φ was measured to be $1.13 \pm 0.12 \times 10^{-2}\,mol\,Einstein^{-1}$ at 254 nm, which was consistent with the study by Marotta et al. (2013) $(1.3 \pm 0.12 \times 10^{-2}\,mol\,Einstein^{-1})$.

It should be noted that the direct photolysis of NAP is limited due to the very high energy requirements for the $\pi \rightarrow \pi^*$ and $\sigma \rightarrow \sigma^*$ or $\sigma \rightarrow \pi^*$ transitions. This is due to two factors, first that the aromatic ring requires a high energy to produce $\pi \rightarrow \pi^*$ transition, and second, the saturated alkane chain $(-CH(CH_3)-)$ requires a high energy to produce $\sigma \rightarrow \sigma^*$ or $\sigma \rightarrow \pi^*$ transition. Only minor dissociation of $-C-COOH$ bond occurs readily under the current UV irradiation (Marotta et al., 2013), which likely leads to a decarboxylation reaction.

3.2. $^\bullet$OH mediated degradation of NAP

The r_{UV} of NAP was measured to be $(2.32 \pm 0.12) \times 10^{-7}\,M\,min^{-1}$, and only 43.6% of NAP was removed after 25 min irradiation. The dark control result showed that NAP does not exhibit degradation in the presence of H_2O_2 within 24 h (Fig. 1). Upon UV irradiation, H_2O_2 is decomposed into $^\bullet$OH with the quantum yield of $1.0\,mol\,Einstein^{-1}$ in pH 3 condition (Table 1) (Legrini et al., 1993). Thus, the apparent degradation rate (k', s^{-1}) of NAP in the UV/H_2O_2 system includes the direct photolysis and $^\bullet$OH oxidation (eqn. (8)).

$$-\frac{dC}{dt} = k'C = (k'_{UV} + k'_{OH})C \tag{8}$$

$$k'_{UV} = \frac{r_{UV}}{C} \tag{9}$$

where $k'_{\bullet OH}$ is the rate constant of $^\bullet$OH oxidation of NAP. The k'_{UV} and $k'_{\bullet OH}$ were fit to a pseudo first−order kinetic model ($R^2 > 0.95$). Fig. 1 demonstrated the degradation rate was significantly enhanced in the presence of $100\,\mu M$ H_2O_2. The k' value was determined to be $0.112\,min^{-1}$, and $^\bullet$OH mediated oxidation accounted for 83% of the NAP degradation kinetics in our UV/H_2O_2 system.

The second−order rate constant (k) value of $^\bullet$OH oxidation of NAP was determined to be $(4.32 \pm 0.04) \times 10^{9}\,M^{-1}\,s^{-1}$ at 298 K using relative rate method. The experimental k value was in a good agreement with the reported value by Feng et al. (2013). However, our measured value is lower than that reported by Huber et al. (2005), which is due to the fact that the dominant species was neutral in our system (pH = 3) and deprotonated NAP in their system (pH = 7). Many studies reported that neutral/ionized species exhibited different reactivity with $^\bullet$OH (Adak et al., 2015). The deprotonated species can form hydrogen bonding with H_2O, thus significantly lowering the activation energy of the reactions and ultimately higher k values (Canonica et al., 2008; Luo et al., 2018a).
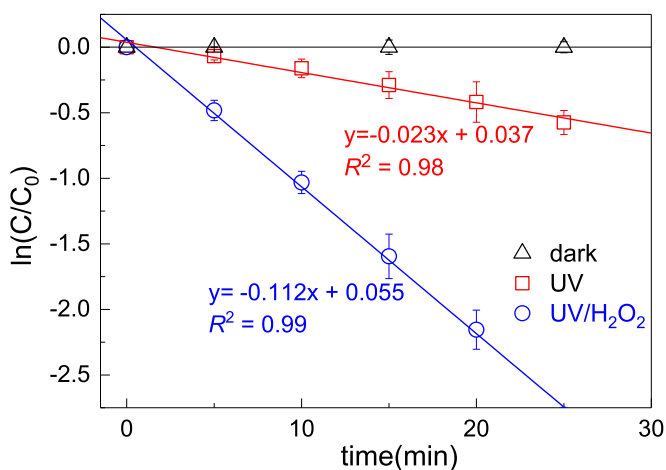

Fig. 1. Time−dependent degradation kinetics of NAP in the UV system with and without H_2O_2 ($[NAP]_0 = 10\,\mu M$, $[H_2O_2]_0 = 100\,\mu M$, pH = 3, and $I_0 = 1.89 \times 10^{-6}$ Einstein $L^{-1}\,s^{-1}$). The degradation kinetics of all the scenarios were fitted to a first−order kinetic model (lines). The error bars were 95% of confidence intervals.

3.3. Theoretical thermodynamics and kinetics

Three reaction pathways, namely, SET, HAT, and RAF, were shown in Fig. 2. All possible reactions of •OH oxidation of NAP are tabulated in Table A16 with calculated enthalpy change ΔH_R° (kcal mol^{-1}), Gibbs free energy change ΔG_R° (kcal mol^{-1}), activation energy $\Delta^\ddagger G^\circ$ (kcal mol^{-1}), imaginary frequencies (cm^{-1}), second–order rate constants k (M^{-1} s^{-1}), and contribution ratio of each pathway in overall k value θ (%) for the •OH oxidation of NAP calculated at SMD/M05−2X/6−311++G**//M05−2X/6−31 + G** level of theory. The free energy profile for the reactions is depicted in Fig. 3.

As shown in Table A16, the SET pathway is thermodynamically unfavorable with positive $\Delta G_R^\circ = 41.1$ kcal mol^{-1}. For the HAT

pathways, ΔH_R° ranges from −35.1 to −17.9 kcal mol^{-1}, and ΔG_R° ranges from −36.1 to −19.9 kcal mol^{-1} (Fig. 3a), indicating that the H−atoms on −CH− (H7), −CH$_3$ (H11), −O−CH$_3$ (H12) and −COOH (H14) sites can be abstracted by •OH. The $\Delta^\ddagger G^\circ$ values of HAT pathways range from 9.84 to 33.5 kcal mol^{-1}. For RAF pathways, ΔH_R° values range from −28.0 to −0.54 kcal mol^{-1}, and ΔG_R° values range from −18.5 to 5.07 kcal mol^{-1} (Fig. 3b). All the reactions are thermodynamically favorable processes ($\Delta G_R^\circ < 0$) except for the addition processes on C13 ($\Delta G_R^\circ = 8.85$ kcal mol^{-1}) and C14 ($\Delta G_R^\circ = 5.07$ kcal mol^{-1}). This is within expectation since addition at these sites would lead to the loss of aromaticity in NAP. The $\Delta^\ddagger G^\circ$ values range from 1.76 to 15.1 kcal mol^{-1}. Since the electron–donating ability of −O−CH$_3$ is higher than that of −CH(CH$_3$)−COOH, the $\Delta^\ddagger G^\circ$ values of •OH addition onto the benzene ring with −O−CH$_3$
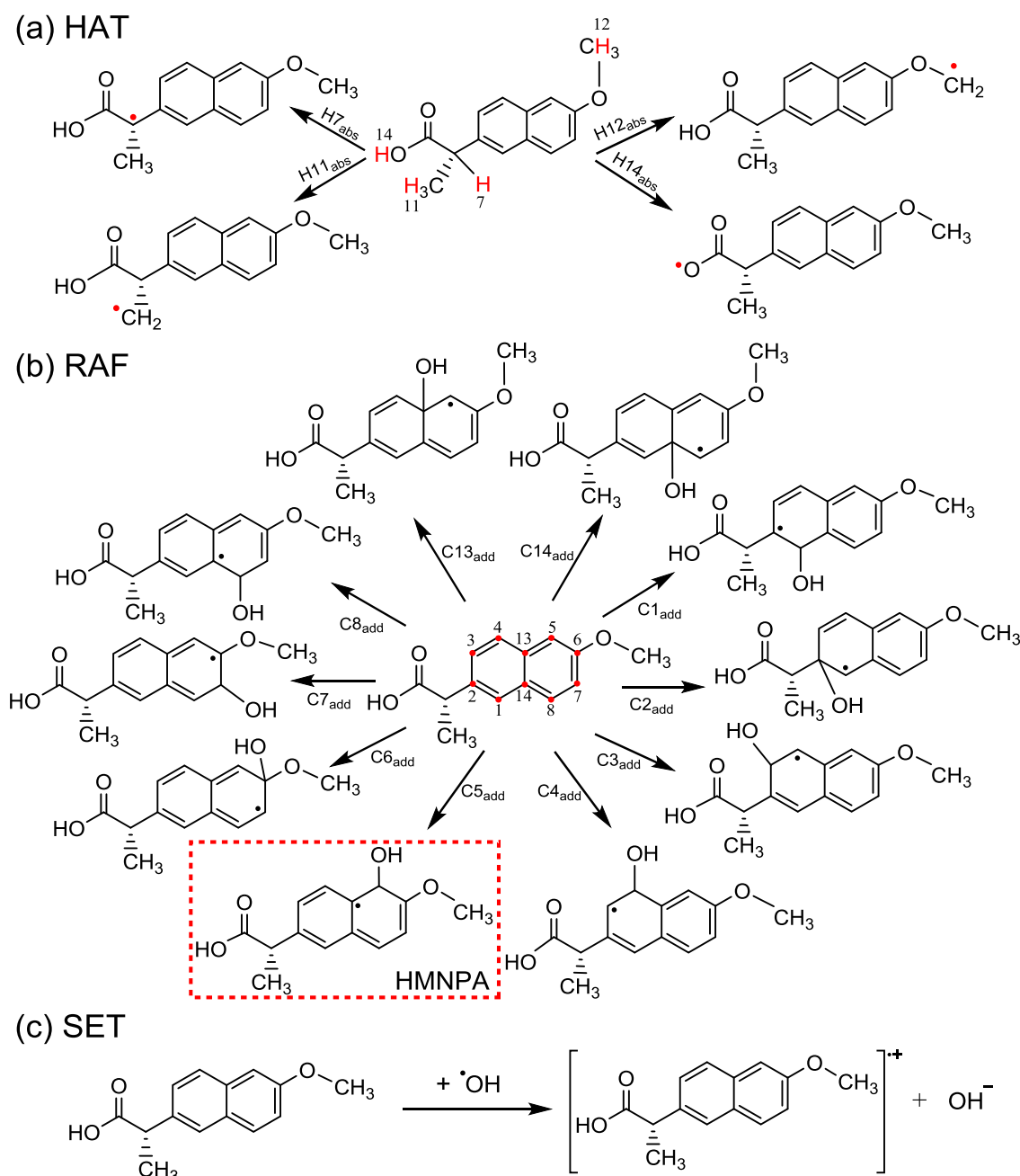

Fig. 2. Three degradation pathways for the reactions of NAP with •OH based on (a) HAT, (b) RAF, and (c) SET pathway. The red dashed frame shows the dominant reaction pathway: •OH addition onto C5 position. (For interpretation of the references to colour in this figure legend, the reader is referred to the Web version of this article.)
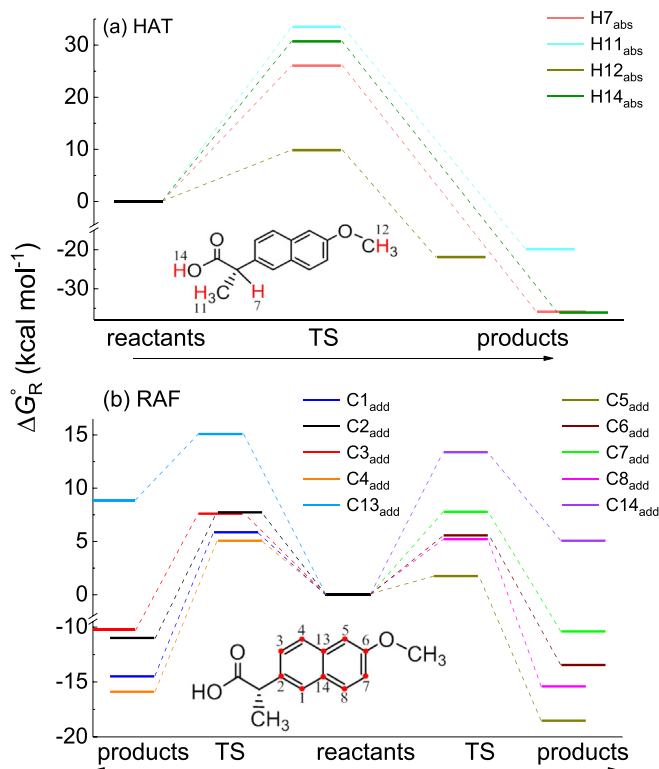
Fig. 3. The potential energy surfaces for the reaction of NAP and •OH via (a) HAT and (b) RAF pathways at SMD/M05−2X/6−311++G**//M05−2X/6−31 + G** level of theory.

substitution (i.e., C5, C6, C7, C8) are lower than the corresponding sites of benzene ring with −CH(CH₃)−COOH substitution (i.e., C1, C2, C3, C4). It should be noted that the $\Delta^{\ddagger}G°$ values of HAT pathways are significantly higher than those of RAF pathways by an average of 17.5 kcal mol⁻¹. The $\Delta^{\ddagger}G°$ of RAF reaction of C5 site, ortho to the electron-donating methoxy group, is significantly lower than other reaction pathways, indicating a primary reaction channel.

The k values of the HAT pathways are from 3.33×10^{-11} to 2.08×10^{6} M⁻¹ s⁻¹ calculated with the Eckart's method. For RAF pathways, their k values are from 9.68×10^{6} to 8.69×10^{9} M⁻¹ s⁻¹. These results indicated that the HAT pathways were almost negligible as compared to the RAF pathways where C5 site was the dominate reaction in •OH oxidation of NAP. The overall k value (1.08×10^{10} M⁻¹ s⁻¹) determined by the model is slightly higher than the k value (($4.32 \pm 0.04) \times 10^{9}$ M⁻¹ s⁻¹) measured experimentally. It should be noted that the Eckart's potential in general provides an accurate representation of the barrier (Miller, 1979). The Γ values of RAF pathway range from 1.01 to 1.49, which is not large due to the low barriers. However, for HAT pathway with activation energy barriers ranging from 9.84 to 33.5 kcal mol⁻¹, the Γ values were from 2.76 to 9.80.

3.4. Mechanistic interpretation for NAP degradation

The unfavorability of the SET reaction is expected to some extent, because the methoxy (−O−CH₃) and ethidene (−CH(CH₃)−) groups on NAP molecule are moderate and weak in electron donating abilities, respectively. Luo et al. (2017b; 2018b) systematically investigated the SET reactions between •OH and 76 aromatic compounds. The SET reaction is thermodynamically favorable for aromatic compounds with strong electron donating moieties, such as oxide, secondary/tertiary amine, and hydroxyl

functional groups.

The •OH can abstract a H atom from −O−CH₃, −CH(CH₃), −COOH and −CH₃ groups forming H₂O and NAP radical (NAP•). The HAT on −O−CH₃ or −CH₃ site forms an unstable methyl radical (−CH₂•), an unfavorable high−energy process, which results in the lower reactivity (Xiao et al., 2017). The reaction with the acidic hydrogen on −COOH group is more complex. The acid group can be involved in hydrogen-bonding which can stabilize the TS complex. However, loss of the hydrogen atom generates a carboxylate radical which is susceptible to a rapid decarboxylation reaction generating a stable benzylic type carbon radical. This reaction pathway has been seen in the observed reaction producing P3, P4, P5 and P6 (Table 2). Loss of H7, the benzylic hydrogen atom, leads to a stable benzylic carbon radical which can then react with an additional •OH in a radical coupling reaction to form the hydroxyl compound seen in reaction product P2 (Table 2). Decarboxylation and dehydration of P2 leads to P3, while decarboxylation and oxidation of P2 leads to P4.

The HOMO and LUMO provide insight into the mechanism of the RAF pathway. The HOMO and LUMO reflect the π−bonding orbital and anti−bonding π^* orbital, respectively (Minakata et al., 2015; Xiao et al., 2017). Minakata et al. (2015) indicated that the LUMO represents the favorability of •OH addition pathway. Fig. A3(a) and (b) show that the HOMO and LUMO are localized on the naphthalene ring. The similarity between HOMO and LUMO indicates that these electron rich regions (naphthalene ring) are more likely attacked by an electrophilic radical (•OH) (DeMatteo et al., 2005). Thus, the C4, C5, and C8 sites are more reactive to •OH with $\Delta^{\ddagger}G°$ values of 5.07, 1.76 and 5.22 kcal mol⁻¹, respectively. The preferred reaction at C5 is due to the electron-donating ability of the methoxy group which increases the electron density on the ring carbons ortho and para to it (i.e., C5 and C7, the para position at C14 has very low reactivity since addition here will result in the loss of aromaticity in the compound). The C5 addition is favored over C7 because the other benzene ring can also act as an electron-donating group to C5. These effects result in the very low $\Delta^{\ddagger}G°$ seen for C5, and the major reaction pathway was RAF pathway in formation of 2−(5−hydroxy−6−methoxynaphthalen−2−yl)propanoic acid (HMNPA).

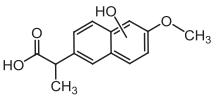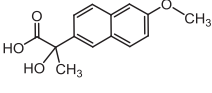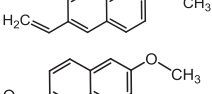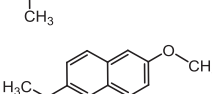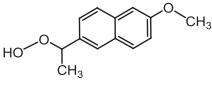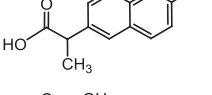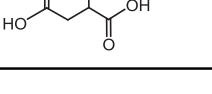### 3.5. Kinetics modelling and degradation intermediates

Although several reaction intermediates have been identified by high performance liquid chromatography−mass spectrum (HPLC/MS) technique from previous studies (Table 2) (Dulova et al., 2017; Gao et al., 2017), the MS information cannot explicitly determine which intermediate is favorable to form and its influence on subsequent •OH oxidation steps (An et al., 2013; Du et al., 2006). This study builds upon the previous work aiming to answer this fundamental question. Based on the theoretical study, the major dominant reaction intermediate was the HMNPA (P1 see Table 2). Therefore, we used this dominant reaction intermediate as an example to elucidate the interplay between parent NAP and formed intermediate during •OH oxidation process.

We speculated that HMNPA exhibits a similar reactivity with •OH as compared to parent NAP. This was based on the extended HOMO and LUMO distribution of HMNPA (see Fig. A3(c) & (d)), especially for LUMO distributions in carboxylic acid group. Since experimentally measuring the k value for the reaction of •OH and HMNPA provided some challenges due to the high cost of synthesis and the extreme complexity of the reaction system, a kinetics modelling technique was used in this study to answer this question.

Fig. 4 demonstrated the NAP and HMNPA concentration evolutions. The fit NAP concentration over time (red line) agreed with the measured ones (red dots). The best model fitting of the kinetics was achieved by applying Mead & Nelder optimization algorithms and standard least squares comparison operator, because this

Table 2
The observed reaction intermediates from the •OH oxidation of NAP.

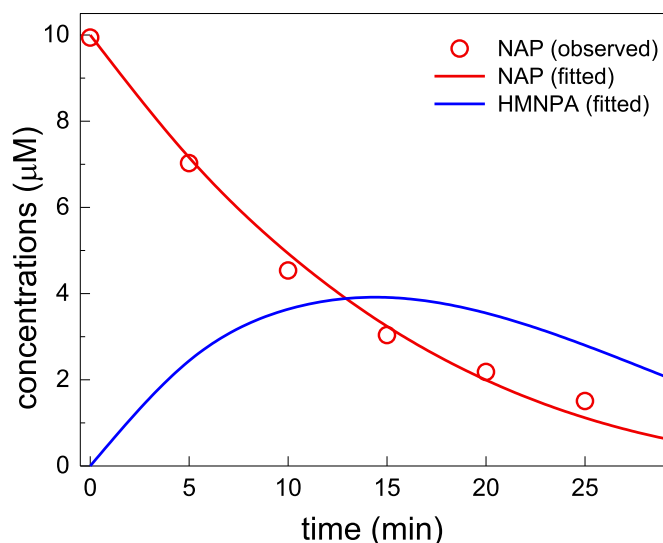| #	Structure	Molecular formula	Molecular weight (g mol^{-1})	m/z	Ref.
P1		$C_{14}H_{15}O_4$	246	247	(Dulova et al., 2017; Gao et al., 2017)
P2		$C_{14}H_{14}O_4$	246	247	(Dulova et al., 2017; Gao et al., 2017)
P3		$C_{13}H_{12}O$	184	185	(Dulova et al., 2017; Gao et al., 2017)
P4		$C_{13}H_{12}O_2$	200	201	(Dulova et al., 2017; Gao et al., 2017)
P5		$C_{13}H_{14}O$	186	187	(Gao et al., 2017)
P6		$C_{13}H_{14}O_3$	218	219	(Dulova et al., 2017)
P7		$C_{13}H_{12}O_3$	216	217	(Dulova et al., 2017)
P8		$C_4H_6O_5$	134	135	(Gao et al., 2017)

Fig. 4. Concentration evolution of NAP and dominant intermediate (HMNPA) in a •OH mediated process under the conditions of [NAP]$_0$ = 10 μM, [H$_2$O$_2$]$_0$ = 100 μM, pH = 3, and I_0 = 1.89 × 10^{-6} Einstein L^{-1} s^{-1}.

combination produced good description of evolution of NAP concentration and reasonable k value. The determination coefficient (R^2) between observed and predicted concentrations of NAP during the experimental was 0.993, and the estimated standard deviations of the modelling error was determined to be 3.12 × 10^{-7} M (6.59%). The modeled concentration of HMNPA increased in the first 15 min and then decreased, indicating that •OH oxidized NAP first followed by HMNPA that starts to compete for •OH in the system with an increase of time. The modeled k value for the reaction between •OH and NAP was 2.53 × 10^9 M^{-1} s^{-1}. The k value of •OH oxidation of HMNPA was modeled to be 2.22 × 10^9 M^{-1} s^{-1}. The HOMO and LUMO distributions of HMNPA (Fig. A3(c) & (d)) are different compared to those of NAP. The energy gap in LUMO and HOMO of HMNPA (6.15 eV) was lower than NAP (6.65 eV), indicating that HMNPA exhibits a higher reactivity than NAP (Minakata et al., 2015; Xiao et al., 2015b). This is likely due to the strong electron-donating properties of the hydroxyl group on the aromatic ring. In addition, the LUMO distribution of HMNPA was extended to carboxylic acid group compared to NAP, suggesting that −COOH group becomes more reactive and could be subject to decarboxylation. It should be noted that we did not calculate the k value of •OH oxidation of HMNPA with the DFT method due to failure of the optimization of their TSs with M05–2X functional.

4. Conclusion

In this study, we combined experimental, theoretical and kinetic modelling approaches to investigate the •OH oxidation of NAP and reaction intermediates in aqueous solution. The UV direct photolysis rate and the k value of •OH oxidation of NAP were measured. The measured k value (4.32 ± 0.04 × 10^9 M^{-1} s^{-1}) was in good agreement with previous reports. The thermodynamic and kinetic behaviors of the initial step reaction pathways were calculated at the SMD/M05–2X/6–311++G**//M05–2X/6–31+G** level of theory. The calculated k value (1.08 × 10^{10} M^{-1} s^{-1}) was higher than the experimentally determined value. In addition, the calculated result shows that the activation barrier of RAF is lower than HAT, and •OH addition at C5 site dominates the reaction. Further, we provided an insight into reaction mechanisms based on electronic

properties of group, activation energy, and the HOMO/LUMO distribution. Finally, a kinetics modelling technique was used to fit the k values and concentration evolution of •OH oxidation of NAP and dominant intermediate (HMNPA). The modelling result is in good agreement with experimental values and suggests that HMNPA exhibits a similar •OH reactivity as compared to NAP, thereby affecting •OH oxidation of NAP. These results can provide further understanding of the salient mechanisms of degradation of NAP using •OH based AOTs and provide guidance in future studies for the removal of NSAIDs and other contaminants of concern by AOTs when such technologies are considered in water and wastewater treatment processes.

Acknowledgements

Appendix A. Supplementary data

Supplementary data related to this article can be found at https://doi.org/10.1016/j.watres.2018.03.002.

References

Adak, A., Mangalgiri, K.P., Lee, J., Blaney, L., 2015. UV irradiation and UV-H₂O₂ advanced oxidation of the roxarsone and nitarsone organoarsenicals. Water Res. 70, 74–85.

An, T.C., Gao, Y.P., Li, G.Y., Kamat, P.V., Peller, J., Joyce, M.V., 2013. Kinetics and mechanism of •OH mediated degradation of dimethyl phthalate in aqueous solution: Experimental and theoretical studies. Environ. Sci. Technol. 48 (1), 641–648.

Balakrishna, K., Rath, A., Praveenkumarreddy, Y., Guruge, K.S., Subedi, B., 2017. A review of the occurrence of pharmaceuticals and personal care products in Indian water bodies. Ecotoxicol. Environ. Saf. 137, 113–120.

Benitez, F.J., Acero, J.L., Real, F.J., Roldan, G., Casas, F., 2011. Comparison of different chemical oxidation treatments for the removal of selected pharmaceuticals in water matrices. Chem. Eng. J. 168 (3), 1149–1156.

Benotti, M.J., Trenholm, R.A., Vanderford, B.J., Holady, J.C., Stanford, B.D., Snyder, S.A., 2008. Pharmaceuticals and endocrine disrupting compounds in US drinking water. Environ. Sci. Technol. 43 (3), 597–603.

Bielski, B.H., Cabelli, D.E., Arudi, R.L., Ross, A.B., 1985. Reactivity of HO₂/O₂⁻ radicals in aqueous solution. J. Phys. Chem. Ref. Data 14 (4), 1041–1100.

Boyd, G.R., Zhang, S., Grimm, D.A., 2005. Naproxen removal from water by chlorination and biofilm processes. Water Res. 39 (4), 668.

Broséus, R., Vincent, S., Aboulfadl, K., Daneshvar, A., Sauvé, S., Barbeau, B., Prévost, M., 2009. Ozone oxidation of pharmaceuticals, endocrine disruptors and pesticides during drinking water treatment. Water Res. 43 (18), 4707–4717.

Brown, R., 1981. A method of calculating tunneling corrections for Eckart potential barriers. J. Res. Natl. Bur. Stand. 86, 357–359.

Buxton, G.V., Greenstock, C.L., Helman, W.P., Ross, A.B., 1988. Critical review of rate constants for reactions of hydrated electrons, hydrogen atoms and hydroxyl radicals (•OH/•O⁻) in aqueous solution. J. Phys. Chem. Ref. Data 17 (2), 513–886.

Canonica, S., Meunier, L., Von Gunten, U., 2008. Phototransformation of selected pharmaceuticals during UV treatment of drinking water. Water Res. 42 (1), 121–128.

Carballa, M., Omil, F., Lema, J.M., Llompart, M.A., GarcıA-Jares, C., RodrıGuez, I., Gómez, M., Ternes, T., 2004. Behavior of pharmaceuticals, cosmetics and hormones in a sewage treatment plant. Water Res. 38 (12), 2918–2926.

Christensen, H., Sehested, K., Corfitzen, H., 1982. Reactions of hydroxyl radicals with hydrogen peroxide at ambient and elevated temperatures. J. Phys. Chem. 86 (9), 1588–1590.

Chuang, Y.-H., Parker, K.M., Mitch, W.A., 2016. Development of predictive models for the degradation of halogenated disinfection byproducts during the UV/H₂O₂ advanced oxidation process. Environ. Sci. Technol. 50 (20), 11209–11217.

Collins, F.C., Kimball, G.E., 1949. Diffusion-controlled reaction rates. J. Colloid Sci. 4 (4), 425–437.

Crittenden, J.C., Hu, S., Hand, D.W., Green, S.A., 1999. A kinetic model for H₂O₂/UV process in a completely mixed batch reactor. Water Res. 33 (10), 2315–2328.

Dai, F., Fan, X., Stratton, G.R., Bellona, C.L., Holsen, T.M., Crimmins, B.S., Xia, X., Thagard, S.M., 2016. Experimental and density functional theoretical study of the effects of Fenton's reaction on the degradation of Bisphenol A in a high voltage plasma reactor. J. Hazard Mater. 308, 419–429.

DeMatteo, M.P., Poole, J.S., Shi, X., Sachdeva, R., Hatcher, P.G., Hadad, C.M., Platz, M.S., 2005. On the electrophilicity of hydroxyl radical: A laser flash photolysis and computational study. J. Am. Chem. Soc. 127 (19), 7094–7109.

Dreuw, A., 2005. Single-reference ab initio methods for the calculation of excited states of large molecules. Chem. Rev. 105 (11), 4009–4037.

Du, Y., Zhou, M., Lei, L., 2006. Role of the intermediates in the degradation of phenolic compounds by Fenton-like process. J. Hazard Mater. 136 (3), 859–865.

Dulova, N., Kattel, E., Trapido, M., 2017. Degradation of naproxen by ferrous ion-activated hydrogen peroxide, persulfate and combined hydrogen peroxide/persulfate processes: The effect of citric acid addition. Chem. Eng. J. 318, 254–263.

Feng, L., van Hullebusch, E.D., Rodrigo, M.A., Esposito, G., Oturan, M.A., 2013. Removal of residual anti-inflammatory and analgesic pharmaceuticals from aqueous systems by electrochemical advanced oxidation processes. A review. Chem. Eng. J. 228 (28), 944–964.

Frisch, M., Trucks, G., Schlegel, H., Scuseria, G., Robb, M., Cheeseman, J., Scalmani, G., Barone, V., Mennucci, B., Petersson, G., 2009. Gaussian 09 (Revision-A. 01). Gaussian, Inc., Wallingford CT.

Galano, A., Alvarez-Idaboy, J.R., 2013. A computational methodology for accurate predictions of rate constants in solution: Application to the assessment of primary antioxidant activity. J. Comput. Chem. 34 (28), 2430–2445.

Gao, Y., Gao, N., Yin, D., Chen, J., 2017. Comparative study of naproxen degradation in water by UV/persulfate and UV/H₂O₂ processes. Desalin. Water Treat 80, 317–325.

Ghernaout, D., 2013. Advanced oxidation phenomena in electrocoagulation process: A myth or a reality? Desalin. Water Treat. 51 (40–42), 7536–7554.

Grebel, J.E., Pignatello, J.J., Mitch, W.A., 2010. Effect of halide ions and carbonates on organic contaminant degradation by hydroxyl radical-based advanced oxidation processes in saline waters. Environ. Sci. Technol. 44 (17), 6822–6828.

Huber, M.M., Gobel, A., Joss, A., Hermann, N., Loffler, D., McArdell, C.S., Ried, A., Siegrist, H., Ternes, T.A., von Gunten, U., 2005. Oxidation of pharmaceuticals during ozonation of municipal wastewater effluents: A pilot study. Environ. Sci. Technol. 39 (11), 4290.

Ianni, J., 2017. Kintecus, Windows Version 6.0. www.kintecus.com.

Koppenol, W.H., Butler, J., van Leeuwen, J.W., 1978. The Haber-Weiss cycle. Photochem. Photobiol. 28 (4-5), 655–658.

Kosjek, T., Heath, E., Krbavcic, A., 2005. Determination of non-steroidal anti-inflammatory drug (NSAIDs) residues in water samples. Environ. Int. 31 (5), 679–685.

Lapworth, D.J., Baran, N., Stuart, M.E., Ward, R.S., 2012. Emerging organic contaminants in groundwater: A review of sources, fate and occurrence. Environ. Pollut. 163 (4), 287–303.

Legrini, O., Oliveros, E., Braun, A., 1993. Photochemical processes for water treatment. Chem. Rev. 93 (2), 671–698.

Lian, L., Yao, B., Hou, S., Fang, J., Yan, S., Song, W., 2017. Kinetic study of hydroxyl and sulfate radical-mediated oxidation of pharmaceuticals in wastewater effluents. Environ. Sci. Technol. 51 (2954–2962).

Liang, C., Wang, Z.-S., Mohanty, N., 2006. Influences of carbonate and chloride ions on persulfate oxidation of trichloroethylene at 20 °C. Sci. Total Environ. 370 (2-3), 271–277.

Luo, S., Wei, Z., Spinney, R., Yang, Z., Chai, L., Xiao, R., 2017a. A novel model to predict gas–phase hydroxyl radical oxidation kinetics of polychlorinated compounds. Chemosphere 172, 333–340.

Luo, S., Wei, Z., Dionysiou, D.D., Spinney, R., Hu, W.-P., Chai, L., Yang, Z., Ye, T., Xiao, R., 2017b. Mechanistic insight into reactivity of sulfate radical with aromatic contaminants through single-electron transfer pathway. Chem. Eng. J. 327, 1056–1065.

Luo, S., Wei, Z., Spinney, R., Zhang, Z., Dionysiou, D.D., Gao, L., Chai, L., Wang, D., Xiao, R., 2018a. UV direct photolysis of sulfamethoxazole and ibuprofen: An experimental and modelling study. J. Hazard Mater. 343, 132–139.

Luo, S., Wei, Z., Spinney, R., Villamena, F.A., Dionysiou, D.D., Chen, D., Tang, C.-J., Chai, L., Xiao, R., 2018b. Quantitative structure–activity relationships for reactivities of sulfate and hydroxyl radicals with aromatic contaminants through single–electron transfer pathway. J. Hazard Mater. 344, 1165–1173.

Manrique-Moreno, M., Suwalsky, M., Villena, F., Garidel, P., 2010. Effects of the nonsteroidal anti-inflammatory drug naproxen on human erythrocytes and on cell membrane molecular models. Biophys. Chem. 147 (1), 53–58.

Marenich, A.V., Cramer, C.J., Truhlar, D.G., 2009. Performance of SM6, SM8, and SMD on the SAMPL1 test set for the prediction of small-molecule solvation free energies. J. Chem. Phys. B 113 (14), 4538–4543.

Marotta, R., Spasiano, D., Somma, I.D., Andreozzi, R., 2013. Photodegradation of naproxen and its photoproducts in aqueous solution at 254nm: A kinetic investigation. Water Res. 47 (1), 373–383.

MATLAB, 2012. Version 8.0. (R2012b). The MathWorks Inc.

Miller, W.H., 1979. Tunneling corrections to unimolecular rate constants, with application to formaldehyde. J. Am. Chem. Soc. 101 (23), 6810–6814.

Minakata, D., Song, W., Mezyk, S.P., Cooper, W.J., 2015. Experimental and theoretical studies on aqueous-phase reactivity of hydroxyl radicals with multiple carboxylated and hydroxylated benzene compounds. Phys. Chem. Chem. Phys. 17 (17), 11796–11812.

Packer, J.L., Werner, J.J., Latch, D.E., McNeill, K., Arnold, W.A., 2003. Photochemical fate of pharmaceuticals in the environment: Naproxen, diclofenac, clofibric acid, and ibuprofen. Aquat. Sci. Res. Across Bound 65 (4), 342–351.

Pereira, V.J., Weinberg, H.S., Linden, K.G., Singer, P.C., 2007. UV degradation kinetics and modeling of pharmaceutical compounds in laboratory grade and surface water via direct and indirect photolysis at 254 nm. Environ. Sci. Technol. 41 (5), 1682–1688.

Sethi, A., Singh, R.P., Prakash, R., Amandeep, 2017. Facile synthesis of corticosteroids

prodrugs from isolated hydrocortisone acetate and their quantum chemical calculations. J. Mol. Struct. 1130.

Sharma, J., Mishra, I., Kumar, V., 2016. Mechanistic study of photo-oxidation of Bisphenol-A (BPA) with hydrogen peroxide (H_2O_2) and sodium persulfate (SPS). J. Environ. Manag. 166, 12−22.

Tang, Y., Li, X.M., Xu, Z.C., Guo, Q.W., Hong, C.Y., Bing, Y.X., 2014. Removal of naproxen and bezafibrate by activated sludge under aerobic conditions: Kinetics and effect of substrates. Biotechnol. Appl. Biochem. 61 (3), 333−341.

Tonelli, A.E., 2014. PLLA in solution: A flexible random-coil or an extended, rather rigid helical polymer. Macromolecules 47 (17), 6141−6143.

Truhlar, D.G., Garrett, B.C., Klippenstein, S.J., 1996. Current status of transition-state theory. J. Phys. Chem. 87 (26), 2664−2682.

Xiao, R., Noerpel, M., Ling Luk, H., Wei, Z., Spinney, R., 2014. Thermodynamic and kinetic study of ibuprofen with hydroxyl radical: A density functional theory approach. Int. J. Quant. Chem. 114 (1), 74−83.

Xiao, R., Zammit, I., Wei, Z., Hu, W., MacLeod, M., Spinney, R., 2015a. Kinetics and mechanism of the oxidation of cyclic methylsiloxanes by hydroxyl radical in the gas phase: An experimental and theoretical study. Environ. Sci. Technol. 49 (22), 13322−13330.

Xiao, R., Ye, T., Wei, Z., Luo, S., Yang, Z., Spinney, R., 2015b. Quantitative structure-activity relationship (QSAR) for the oxidation of trace organic contaminants by sulfate radical. Environ. Sci. Technol. 49 (22), 13394−13402.

Xiao, R., Gao, L., Wei, Z., Spinney, R., Luo, S., Wang, D., Dionysiou, D.D., Tang, C.J., Yang, W., 2017. Mechanistic insight into degradation of endocrine disrupting chemical by hydroxyl radical: An experimental and theoretical approach. Environ. Pollut. 231, 1446−1452.

Yang, Z., Luo, S., Wei, Z., Ye, T., Spinney, R., Chen, D., Xiao, R., 2016. Rate constants of hydroxyl radical oxidation of polychlorinated biphenyls in the gas phase: A single−descriptor based QSAR and DFT study. Environ. Pollut. 211, 157−164.

Yang, Z., Su, R., Luo, S., Spinney, R., Cai, M., Xiao, R., Wei, Z., 2017. Comparison of the reactivity of ibuprofen with sulfate and hydroxyl radicals: An experimental and theoretical study. Sci. Total Environ. 590−591, 751−760.

Ye, T., Wei, Z., Spinney, R., Tang, C.-J., Luo, S., Xiao, R., Dionysiou, D.D., 2017. Chemical structure-based predictive model for the oxidation of trace organic contaminants by sulfate radical. Water Res. 116, 106−115.

Zepp, R.G., 1978. Quantum yields for reaction of pollutants in dilute aqueous solution. Environ. Sci. Technol. 12 (3), 327−329.

Zhang, Y., Price, G., Jamieson, R., Burton, D., Khosravi, K., 2017. Sorption and desorption of selected non-steroidal anti-inflammatory drugs in an agricultural loam-textured soil. Chemosphere 174, 628−637.

Zhao, Y., Truhlar, D.G., 2008. The M06 suite of density functionals for main group thermochemistry, thermochemical kinetics, noncovalent interactions, excited states, and transition elements: Two new functionals and systematic testing of four M06-class functionals and 12 other functionals. Theor. Chem. Accounts 120 (1−3), 215−241.

Zhao, Y., Schultz, N.E., Truhlar, D.G., 2006. Design of density functionals by combining the method of constraint satisfaction with parametrization for thermochemistry, thermochemical kinetics, and noncovalent interactions. J. Chem. Theor. Comput. 2 (2), 364−382.

Zhou, Y., Liu, X., Tang, L., Zhang, F., Zeng, G., Peng, X., Luo, L., Deng, Y., Pang, Y., Zhang, J., 2017. Insight into highly efficient co-removal of p-nitrophenol and lead by nitrogen-functionalized magnetic ordered mesoporous carbon: performance and modelling. J. Hazard Mater. 333, 80−87.